Environmental Changes in $MoTe_2$ Excitonic Dynamics by Defects-Activated Molecular Interaction

Bin Chen,[†,⊥] Hasan Sahin,[‡,⊥] Aslihan Suslu,[†] Laura Ding,[§] Mariana I. Bertoni,[§] F. M. Peeters,[‡] and Sefaattin Tongay*[,†]

[†]School for Engineering of Matter, Transport and Energy, and [§]School of Electrical Computer and Energy Engineering, Arizona State University, Tempe, Arizona 85287, United States and [‡]Department of Physics, University of Antwerp, Groenenborgerlaan 171, Antwerpen B-2020, Belgium. [⊥]B. Chen and H. Sahin contributed equally to this work.

ABSTRACT

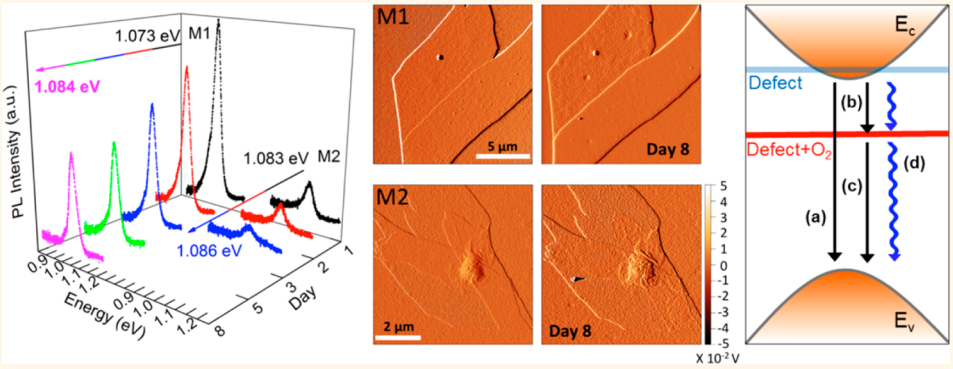

Monolayers of group VI transition metal dichalcogenides possess direct gaps in the visible spectrum with the exception of $MoTe_2$, where its gap is suitably located in the infrared region but its stability is of particular interest, as tellurium compounds are acutely sensitive to oxygen exposure. Here, our environmental (time-dependent) measurements reveal two distinct effects on $MoTe_2$ monolayers: For weakly luminescent monolayers, photoluminescence signal and optical contrast disappear, as if they are decomposed, but yet remain intact as evidenced by AFM and Raman measurements. In contrast, strongly luminescent monolayers retain their optical contrast for a prolonged amount of time, while their PL peak blue-shifts and PL intensity saturates to slightly lower values. Our X-ray photoelectron spectroscopy measurements and DFT calculations suggest that the presence of defects and functionalization of these defect sites with O_2 molecules strongly dictate their material properties and aging response by changing the excitonic dynamics due to deep or shallow states that are created within the optical band gap. Presented results not only shed light on environmental effects on fundamental material properties and excitonic dynamics of $MoTe_2$ monolayers but also highlight striking material transformation for metastable 2D systems such as WTe_2, silicone, and phosphorene.

KEYWORDS: $MoTe_2$ · excitons · photoluminescence · environmental stability · 2D materials

Two-dimensional (2D) semiconducting transition metal dichalcogenides (sTMDs) are emerging as a new class of materials with novel properties that are potentially important for a wide range of applications in optoelectronics, energy harvesting conversion, and photonics technologies.[1−3] 2D sTMDs involving group VI elements (Mo and W) and chalcogens (S and Se) are of particular interest owing to their unique properties that are significantly different from their bulk counterparts: For example, when isolated to monolayers, they become direct gap semiconductors where photons are absorbed and emitted rather strongly at energies from 1.5 eV ($MoSe_2$) to 2.05 eV (WS_2),[4−6] and the light emission can be modulated within orders of magnitude by surface engineering and chemical-organic doping techniques.[7,8] In the confinement limit, they possess rather unusual effects and properties such as valley-selective photonics, rich excitonic phenomena, piezoelectricity, second-harmonic

* Address correspondence to Sefaattin.Tongay@asu.edu.

Received for review February 10, 2015 and accepted April 13, 2015.

Published online April 13, 2015
10.1021/acsnano.5b00985

© 2015 American Chemical Society

generation, and sensitivity to surrounding dielectrics medium.[9−12]

Recently, optical studies on few-layer and monolayer $MoTe_2$ have revealed that $MoTe_2$ also undergoes indirect to direct transition in the confinement limit where $MoTe_2$ monolayers become direct gap semiconductors at 1.05 eV, and their overall properties are currently largely unknown.[13,14] Despite such similarities among group VI TMDs, tellurium-containing TMDs chemically differ in a way that their interaction with the environment is complex due to the oxidative properties of tellurium. For instance, interaction between O_2 and tellurium readily results in α-TeO_2 (paratellurite), whereas oxidization of selenium requires multichemical steps involving H_2O_2 and HNO_3.[15]

Here, we demonstrate that the properties of monolayer $MoTe_2$ undergo unusual changes in ambient conditions on a time scale that is on the order of days to a week, which is in stark contrast to other group VI TMDs. After exposing monolayers to air, the optical contrast of the monolayers decreases significantly, and eventually it becomes undetectable, as if the samples were decomposing in air. However, atomic force microscopy (AFM) and Raman spectroscopy measurements show that monolayers are structurally still intact without signs of environmental deterioration (decomposition) even though the photoluminescence (PL) signal gradually decreases and blue-shifts during the aging period. Interestingly, our measurements show that the aging effects are strongly correlated to the magnitude of the initial luminescence measured on freshly exfoliated monolayer $MoTe_2$, suggesting that the variations in the intrinsic density of defects play a significant role in their environmental stability. Our DFT calculations and X-ray photoelectron spectroscopy (XPS) measurements reveal that the presence of chalcogen vacancies creates chemically active sites, promotes local oxidization (defect functionalization), and creates deep and shallow states within the optical band gap.

RESULTS AND DISCUSSION

Monolayers of $MoTe_2$ and Their Optical/Vibrational Properties. Monolayers of $MoTe_2$ flakes were exfoliated from synthesized bulk crystals on piranha-etched 300 nm SiO_2/Si substrates using mechanical exfoliation (Figure 1a). AFM measurements show that the monolayers are atomically flat (Figure 1d) and ~0.7 nm thick. Our infrared PL measurements displayed strong light emission at ~1.07 eV (Figure 1b), which is larger than their bulk values (indirect gap at 0.83 eV), as determined by our UV−vis photospectroscopy measurements (Figure S1). This implies that the $MoTe_2$ goes through an indirect to direct gap transition[13] when going from bulk to monolayers just like other members of the group VI TMDs. The experimentally measured gap values agree reasonably with our DFT calculations (Figure 1c). Calculated spin−orbit coupling (SOC) in the valence band minimum (VBM) and conduction band maximum (CBM) at the K symmetry point is around $\Delta E_{SOC\text{-}VBM} \approx 216$ meV and $\Delta_{SOC-CBM} \approx 35$ meV, respectively. Unlike TMDs, light emission related to B exciton complexes—associated with relaxation from the CBM to theh SOC band (of VBM)—is not prominent except for a few samples (Figure S2) where the B exciton feature was observed 0.3 eV above

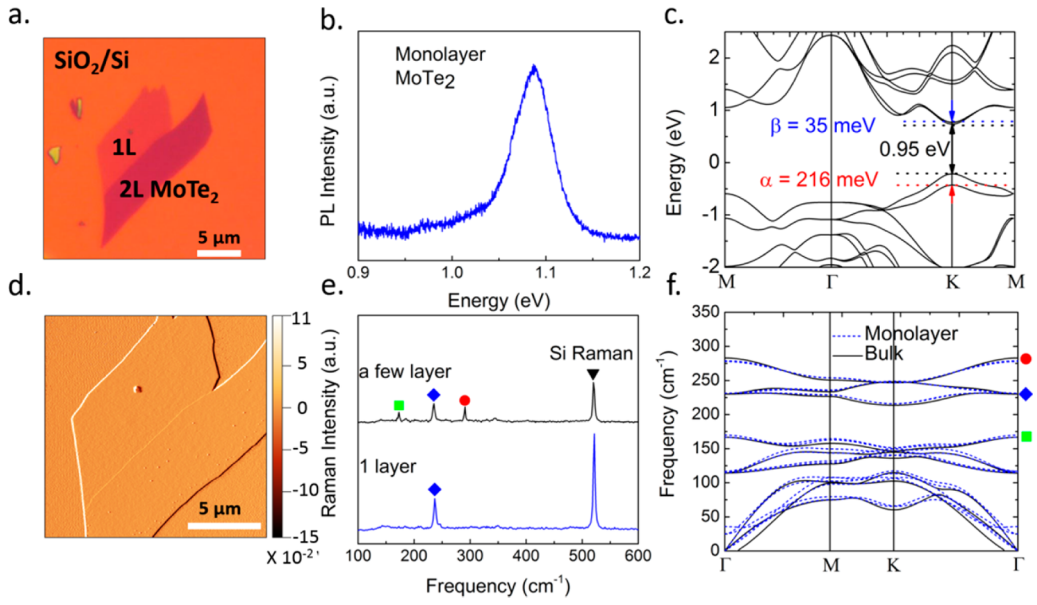

Figure 1. (a) Optical image and (b) photoluminescence spectrum taken on monolayer $MoTe_2$ sheets on 300 nm SiO_2/Si substrates. (c) Calculated band structure of $MoTe_2$ using DFT calculations where α and β are the spin−orbit splitting values for VBM and CBM. (d) Atomic force microscopy image taken from $MoTe_2$ monolayers. (e) Measured Raman spectrum of monolayer and few-layer $MoTe_2$ and (f) calculated vibrational spectrum of monolayer and bulk $MoTe_2$.

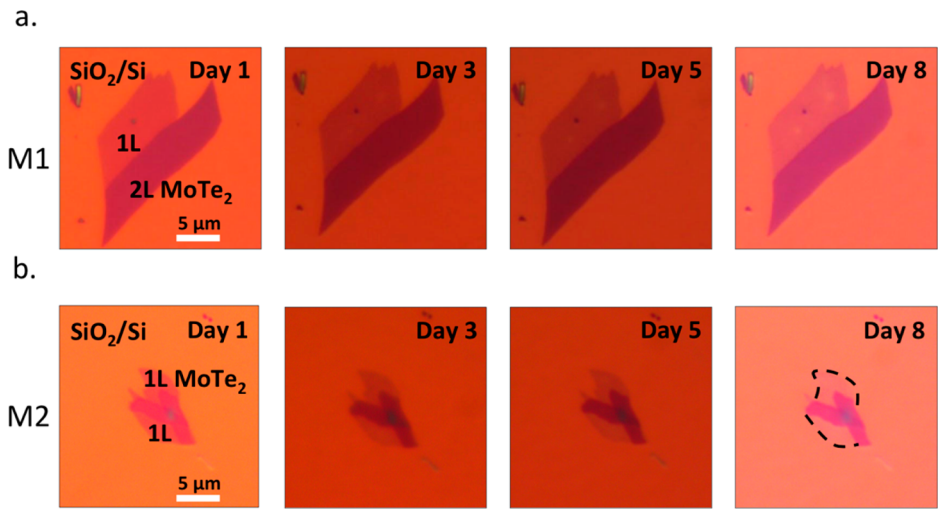

Figure 2. Time-dependent optical images taken from $MoTe_2$ monolayers deposited onto 300 nm/SiO_2/Si substrates for (a) sample M1 and (b) sample M2. Day 1 and day 8 correspond to freshly exfoliated and exposed samples, respectively.

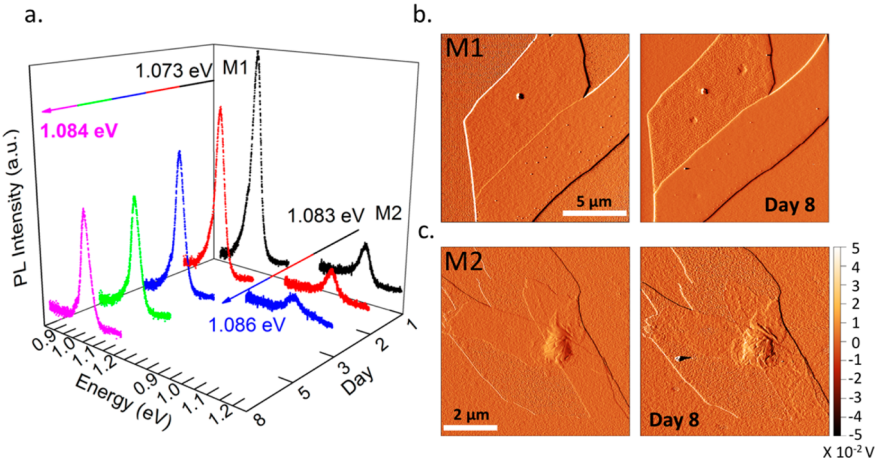

Figure 3. Time-dependent (a) photoluminescence measurements on samples M1 and M2 from day 1 through day 8 and (b) atomic force microscopy images taken from M1 and (c) M2 freshly exfoliated and after 8 days' exposure to air.

the A exciton emission (CBM → VBM, *i.e.*, main PL emission) line, which is also consistent with the DFT calculations.

The measured Raman spectrum and calculated vibrational structure on $MoTe_2$ closely match each other, with the three prominent Raman modes at 170, 235, and 289 cm^{-1} identified as A^1_g, E^1_{2g}, and B_{2g} modes, respectively. Here, the A^1_g mode is only in resonance (Raman scattering cross-section is enhanced) for laser excitations with 633 nm,[13] and in our measurements (488 and 532 nm) this mode cannot be detected. Similarly, the B_{2g} mode involves atoms in the adjacent layers; therefore confinement to monolayers reduces the symmetry and the B_{2g} mode becomes undefined, leaving only one distinct peak at 235 cm^{-1} (in-plane E^1_{2g} mode); this, *i.e.*, observing a single Raman peak at 235 cm^{-1}, allows us to identify monolayers using Raman spectroscopy techniques (Figure 1e,f).

Environmental Effects on Optical Properties of Monolayer $MoTe_2$. In Figure 2, we show time-dependent optical images from $MoTe_2$ monolayers that were exfoliated from the same $MoTe_2$ crystal. Since $MoTe_2$ monolayers displayed two different ranges of PL intensities, for the sake of clarity, we categorized a large collection of samples by their total emission intensity into two groups, namely, M1 and M2, which correspond to "highly" and "weakly" luminescent flakes, respectively (see Figure 3a and discussion in the paragraph below). On the basis of our observations, the optical contrast of sample M1 does not change with time (within 8 days and longer), but unexpectedly, for M2, it decreases by orders of magnitude and eventually the sample disappears (Figure 2b far right), implying that M2 flake is environmentally unstable compared to M1. However, AFM measurements performed on M1 and M2 show virtually no change after 8 days (Figure 3b,c), as their thickness and surface morphology remain unchanged. *This implies that monolayers of $MoTe_2$ do not deteriorate/decompose in air, but instead their optical properties are largely affected.*

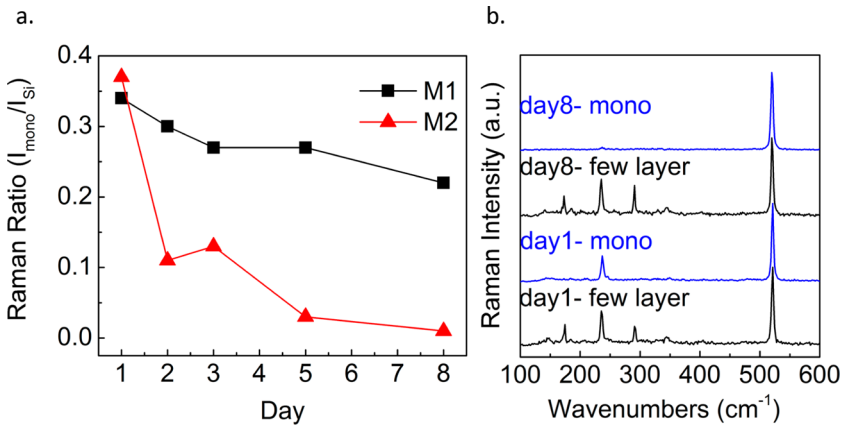

Figure 4. (a) Changes in the relative E^1_{2g} mode peak intensities (I_{mono}/I_{Si}) as a function of time. (b) Raman spectra collected from both monolayer and few-layer $MoTe_2$ on day 1 (freshly exfoliated) and day 8.

Our near-IR micro-PL measurements performed on a large number of samples reveal that samples categorized into M1 have strong light emission (PL), whereas M2 samples are weakly luminescent, as shown in Figure 3a (day 1). The presence of defects in semiconductors is known to affect the intensity of photoluminescence due to changes in the radiative to nonradiative recombination ratio as well as creation of bound and other exciton complexes.[16] These effects are greatly enhanced in 2D samples due to confinement effects, and observed PL variations are thus related to variations in native defect densities created during the crystal growth process. In addition to our homemade crystals, for comparison, we also used commercially available crystals from three different vendors and found similar results. PL measurements show that the intensity of M1 emission initially decreases during the first 1- to 3-day period, until gradually saturating to values 20−50% lower compared to initial values and then always remains luminescent after a week (Figure 3a) and even months (see Figure S3). In contrast, PL emission from the M2 sample starts at much lower values and quickly vanishes within 1−3 days. Comparison between the fwhm of PL peaks for M1 and M2 starts relatively similar, and by aging the M2 sample broadens from 50 meV to ∼70 meV. In addition to PL intensity changes, the PL peak position of the M1 sample blue-shifts from ∼1.073 eV to 1.084 eV, whereas the PL peak of M2, which is initially located at higher energies (∼1.08 eV), remains almost constant with time. These changes will be discussed later in the article in the Discussion section.

As opposed to large differences in their PL intensities, freshly exfoliated M1 and M2 monolayers have relatively close Raman signals (day 1 in Figure 4a). Unlike light emission, the presence of defects does not directly affect Raman E^1_{2g} mode peak intensities but instead only broadens the fwhm of the peak by relaxing the $\Gamma = 0$ condition as observed in our measurements (M1 displays slightly narrower Raman fwhm compared to M2 by 0.2−0.5 cm^{-1}). Similar to observed PL trends, the Raman peak intensity for M2 decreases faster than M1, but the E^1_{2g} mode of $MoTe_2$ still remains detectable (Figure 4a,b) by Raman spectroscopy techniques, which agrees with our AFM measurements, where optically invisible monolayers were found to be structurally intact (Figure 3b,c). Interestingly, Raman spectra (Figure 4b) and optical contrast images (Figure 2a,b) of a few layers of $MoTe_2$ (darker regions in the optical images) remain completely unchanged, and hence we speculate that the additional layers of $MoTe_2$ might improve their resilience against the aging process possibly by minimizing (limiting) the interaction between monolayers and gas/molecules to the outermost layer.

Molecular Interaction on Monolayer $MoTe_2$ Surface. To understand the underlying mechanism for the aging process, we employed density functional theory calculations and microresolution X-ray photoelectron spectroscopy to explore the interaction between monolayer $MoTe_2$ and common gas molecules present in air. On the basis of our DFT calculations, atomic H, N, and O have a tendency to form chemical bonding with a binding energy (E_b) of around a couple of electronvolts. Experimentally, however, this is a rather unlikely case, as these monatomic species do not naturally exist in air and their presence relies on the plasma processing techniques (*i.e.*, breaking bonds). The interaction with air-abundant molecules such as N_2 (78%) and O_2 (21%) leads to weak physisorption ($E_b \approx 35-64$ meV), which is comparable to room-temperature energy, and implies that "absorbed" molecules would almost immediately desorb from the $MoTe_2$ surface. Interestingly, the presence of defects strongly enhances the binding energy: For example, interaction at the defect sites, such as tellurium vacancies, which is identified by our XPS measurements and discussed below, yields an order of magnitude larger binding between monolayer $MoTe_2$ and O_2 ($E_b \approx 166$ meV) compared to the pristine case, and thus quasi-chemisorption and/or

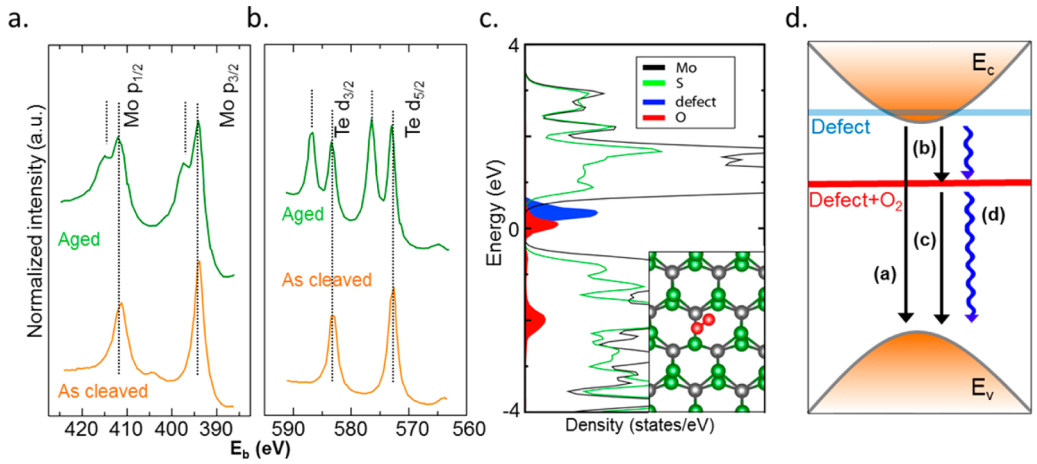

Figure 5. X-ray photoelectron spectroscopy (XPS) data taken on freshly exfoliated and aged surfaces around (a) Mo 3p and (b) Te 3d peaks. (c) Density of states calculation for $MoTe_2$ monolayers showing the local density of states around defects (blue) and interaction with O_2 molecules through defect sites (red). (d) Diagram displaying the effects of defects and O_2 absorption at the defect site on the exciton relaxation dynamics.

physisorption takes place on the surface. As shown in Figure 5c, in the relaxed configuration, O_2 interacts in a way that the upper O atom is interacting with two neighboring Te atoms, as the lower O atom is located on top of the center of the vacancy. Our charge analysis shows that a charge transfer of 0.2 electron occurs from $MoTe_2$ to O_2, leaving $MoTe_2$ p-doped. As opposed to the O_2 case, N_2 molecules do not form strong bonding at the defect site and its binding energy still remains around ~10 meV. However, DFT calculations also predict that H_2O molecules in air (0.4% at 38% humidity) strongly interact with Te-defect sites, but unlike the O_2 case, this binding process relies heavily on splitting H_2O molecules, which leaves Te−O and Te−OH bonds on the surface. Considering the relatively low H_2O concentration in air (compared to O_2) and strict conditions on splitting H_2O molecules, we treat the $H_2O/MoTe_2$ interaction as a distant possibility and focus our efforts on the O_2−$MoTe_2$ interaction.

We tested the interaction between O_2 and the $MoTe_2$ surface using environmental XPS measurements, which were taken at the same spatial location immediately after *in situ* cleavage (day 1) and after aging the surface in air for a week (day 7). We note that within the sensitivity of our XPS measurements (±2−4 at. %) the Te/Mo compositional ratio ranges from 1.9 to 2.01, suggesting that local chalcogen vacancy density might spatially vary in accord with large PL intensity variations (Figure 3a) that were associated with changes in the local density of defects earlier in the article. Comparison between day 1 and 7 shows that the oxygen 1s (O_{1s}) peak becomes apparent in the broad-range XPS spectrum (Figure S4), but this supportive finding is not conclusive, as any arbitrary sample, including the ones (such as graphite) that do not have any oxidization state, would also develop a similar O_{1s} peak after ambient exposure. Indeed, hard evidence for oxidization requires Mo and Te peaks (binding energies E_b) to develop new peaks that are specific to oxidization states such as MoO_3, MoO_2, and TeO_2. It is immediately evident in the XPS spectrum around Mo 3p peaks, Figure 5a, that new features appear at 415 and 398.5 eV, which are in close proximity to Mo $3p_{1/2}$ (411 eV) and $3p_{3/2}$ peaks (394 eV). These new peaks are associated with the oxidization state 6^+ of Mo (like in MoO_3).[17] Similarly, Te $3d_{3/2}$ and $3d_{5/2}$ peaks (Figure 5b) consist of juxtaposition of Te in $MoTe_2$ (583.3 and 572.9 eV) and oxidized Te, like in TeO_2 (587.2 and 576.6 eV) peaks. The results show that after O_2 interacts at the Te-defect sites Mo−O and Te−O bonds (XPS peaks) are formed, and they exist together with the Mo−Te bonds, implying that O_2 molecules are actually embedded into the defect site to form these bonds, which is consistent with our DFT calculations, which predict that O_2 molecules bind to neighboring Mo and Te atoms. Hence, XPS measurements convincingly demonstrate that the surface heavily interacts with O_2, leaving monolayers structurally intact but in a partially oxidized state.[17]

Changes in the Band Structure and Discussion. On the basis of our results, we focus our discussion on the band structure in three different cases: (i) pristine $MoTe_2$, (ii) defected $MoTe_2$, and (iii) O_2 absorption at the defect site. Since the presence of defects breaks the translational symmetry, the band structure calculations require construction of large unit cells, and in such cases plotting density of states (DOS), as opposed to band structure, allows a convenient way to predict changes in the material properties. In Figure 5c, we show the calculated DOS for monolayer $MoTe_2$ (black solid line) as well as the change in DOS due to formation of defects (blue) and defect site−O_2 interaction (red). The presence of defects creates broadly distributed (fmwh ≈ 0.28 eV) discrete states located mostly around the CBM, which do not affect the fundamental gap values. However, once O_2 molecules are absorbed at the defect sites, these discrete levels transform into

deep-level states located approximately ~0.4 eV below the CBM (Figure 5c). These can be schematically summarized in Figure 5d, where defect- and O_2-absorption-related levels are highlighted by blue and red lines, respectively.

In general, for direct gap crystalline semiconductors, radiative recombination of photogenerated electrons and holes is the dominant process, but the presence of imperfections such as defects, impurities, and/or surface states results in finite nonradiative (NR) recombination. If the density of extrinsic imperfections is large, then the NR recombination process starts to surpass the radiative emission, and the overall photoluminescence signal thus becomes much weaker compared to the relatively perfect (intrinsic) material. For instance, large differences in measured PL intensities from M1 and M2 sample sets are likely to be related to these extrinsic variations, *i.e.*, density of Te vacancy, which leads to different radiative to nonradiative recombination rates that arise from variations in their defect densities (M1 is less defective and thus more luminescent).

Once O_2 molecules (and maybe other molecules in the ambient such as H_2O) interact with the defected $MoTe_2$ monolayers (Figure 5c inset), characteristic energy levels falling within the optical band gap largely change (Figure 5c). For example, in vacuum conditions (molecular interaction is avoided), the energy levels of these defects would be located in close proximity to the CBM, which can be treated as shallow states (Figure 5d), but once these sites are functionalized with O_2 molecules, the energy levels shift to the midgap region (Figure 5c,d) and they become deep-level states.

Usually, recombination processes involving deep-level traps are nonradiative in nature with negligible radiative emission from these transitions (*i.e.*, process (d) is much faster than process (c) in Figure 5d) and weak PL emission from M2 samples still originates from (weaker) radiative emission from CBM to VBM (process (a) in Figure 5d). From this perspective, the samples with the highest density of defects (such as M2) would initially have localized states around the CBM, and an interaction with O_2 pushes states into deep levels, which results in nonluminescent properties (Figure 3a). This implies that M2 samples have low starting PL intensity due to a large number of defects, and in time it further decreases due to formation of deep states. On the other hand, M1 samples contain a fewer number of defects (which is why their initial PL intensity is stronger compared to M2) and interaction with O_2 gradually can create only a limited number of deep states (defect density is the limiting factor) and saturates the PL intensity to lower values. Here, we also highlight another nonradiative process, Auger nonradiative recombination, which typically becomes dominant for materials with deep-level states and dopants (doped semiconductors). Since O_2—defect site interaction withdraws 0.2 e^- from $MoTe_2$, positively doping $MoTe_2$, it increases the probability of an electron finding a hole to recombine with and a second hole to dissipate energy, *i.e.*, increases the Auger scattering cross-section,[18] which might also contribute to the above nonradiative combination processes.

Lastly, we also point out that the initial PL emission from M2 samples peaks at approximately 10 meV higher than M1 samples, and similarly the M1 PL peak blueshifts by aging (Figure 3a). First, we recognize that the observed changes are rather small compared to room temperature (26 meV), at which the measurements were performed, and therefore this most likely is not directly related to the excitonic interactions. Since O_2—defect site interaction results in net charge transfer (doping), the electrical conductivity and thus thermal conductivity (within the Weidemann—Franz law) are increased. This, in return, minimizes the laser-induced local heating effect, which is considerably significant in the IR materials, and the PL peak of pristine (M1) samples appears at lower energies due to local heating and by aging shifts to the higher energies comparable to M2 samples. Alternatively, small shifts might be related to changes in the magnitude of spin—orbit coupling (~30 meV Figure 1c) at the conduction band by O_2—defect site interaction.

CONCLUSIONS

To summarize, time-dependent measurements performed on $MoTe_2$ monolayers show that weakly luminescent samples optically disappear within a couple of days as if they are decomposing in air, but AFM measurements suggest that monolayers are structurally stable. In addition to optical contrast, their vibrational response, PL intensity, PL peak position, and band structure largely change. Experimental and theoretical data suggest that interactions mostly between intrinsic defects and O_2 molecules dictate their properties and environmental stability. Overall the results shed light on the environmental stability of not only unique IR range group VI TMDs ($MoTe_2$) but possibly other environmentally metastable 2D systems such as silicene, WTe_2, and phosphorene that are naturally prone to surface effects due to their high surface to volume ratio.

METHODS AND EXPERIMENTAL SECTION

Sample Preparation. Monolayer $MoTe_2$ flakes were exfoliated from bulk crystals onto a Si wafer coated with 300 nm of SiO_2. Before use, Si/SiO_2 wafers were treated in piranha solution for 5—24 h.

Micro-PL/Raman. Measurements were performed using a Renishaw PL/Raman system. The laser wavelength for Raman was 488 nm, and that for PL was 532 nm, both of which were focused onto the sample (spot diameter of ~1—2 μm) using

excitation power up to 2−5 μW. NIR and vis objective lenses were used in the PL and Raman setup.

Atomic Force Microscopy. Monolayer $MoTe_2$ was scanned on a Bruker D3000 scanning probe microscope in ambient environment. The scanning rate was 1 Hz, and the resolution was set to 512 × 512. The data were processed by Gwyddion software.

Density Functional Theory Calculations. For the bulk and single-layer $MoTe_2$ single crystals, the optimized lattice parameters and electronic structure were determined by performing *ab initio* calculations in the framework of density functional theory, as carried out within the Vienna *ab initio* simulation package (VASP),[19,20] with the projector augmented wave (PAW) method.[21] The generalized gradient approximation (GGA) of Perdew−Burke−Ernzerhof (PBE) was used for the exchange−correlation potential.[22] A high plane-wave kinetic energy cutoff of 500 eV was adopted. Brillouin zone integration was performed using a 27 × 27 × 1 and 27 × 27 × 5 Monkhorst−Pack mesh for single-layer and bulk structures, respectively. To avoid weak interactions between adjacent single layers of $MoTe_2$, calculations are performed with a large unit cell including a 12 A vacuum. Ground states and total energies were obtained after full geometry relaxation with a force convergence criterion of 10^{-5} eV. For further examination of dynamical stability and for the determination of vibrational characteristics of bulk and single-layer $MoTe_2$, phonon frequencies were calculated throughout the Brillouin zone using the small displacement methodology with the forces obtained from VASP.[23]

Conflict of Interest: The authors declare no competing financial interest.

Acknowledgment. This work was supported by the Arizona State University seeding program. The authors thank Hui Cai and Kedi Wu for useful discussions. We gratefully acknowledge the use of facilities at the LeRoy Eyring Center for Solid State Science at Arizona State University. This work was supported by the Flemish Science Foundation (FWO-Vl) and the Methusalem Foundation of the Flemish government. H.S. is supported by a FWO Pegasus Long Marie Curie Fellowship.

Supporting Information Available: Experimental specifics, materials preparation including MoS_2, $MoSe_2$, and WSe_2, and information on annealing effects. This material is available free of charge *via* the Internet at http://pubs.acs.org.

REFERENCES AND NOTES

1. Akinwande, D.; Petrone, N.; Hone, J. Two-Dimensional Flexible Nanoelectronics. *Nat. Commun.* **2014**, 5.
2. Wang, Q. H.; Kalantar-Zadeh, K.; Kis, A.; Coleman, J. N.; Strano, M. S. Electronics and Optoelectronics of Two-Dimensional Transition Metal Dichalcogenides. *Nat. Nanotechnol.* **2012**, *7*, 699–712.
3. Radisavljevic, B.; Radenovic, A.; Brivio, J.; Giacometti, V.; Kis, A. Single-Layer MoS_2 Transistors. *Nat. Nanotechnol.* **2011**, *6*, 147–150.
4. Mak, K. F.; Lee, C.; Hone, J.; Shan, J.; Heinz, T. F. Atomically Thin MoS_2: A New Direct-Gap Semiconductor. *Phys. Rev. Lett.* **2010**, *105*, 136805.
5. Splendiani, A.; Sun, L.; Zhang, Y.; Li, T.; Kim, J.; Chim, C.-Y.; Galli, G.; Wang, F. Emerging Photoluminescence in Monolayer MoS_2. *Nano Lett.* **2010**, *10*, 1271–1275.
6. Tongay, S.; Zhou, J.; Ataca, C.; Lo, K.; Matthews, T. S.; Li, J.; Grossman, J. C.; Wu, J. Thermally Driven Crossover from Indirect toward Direct Bandgap in 2D Semiconductors: $MoSe_2$ *versus* MoS_2. *Nano Lett.* **2012**, *12*, 5576–5580.
7. Tongay, S.; Zhou, J.; Ataca, C.; Liu, J.; Kang, J. S.; Matthews, T. S.; You, L.; Li, J.; Grossman, J. C.; Wu, J. Broad-Range Modulation of Light Emission in Two-Dimensional Semiconductors by Molecular Physisorption Gating. *Nano Lett.* **2013**, *13*, 2831–2836.
8. Mouri, S.; Miyauchi, Y.; Matsuda, K. Tunable Photoluminescence of Monolayer MoS_2 *via* Chemical Doping. *Nano Lett.* **2013**, *13*, 5944–5948.
9. Kim, J.; Hong, X.; Jin, C.; Shi, S.-F.; Chang, C.-Y. S.; Chiu, M.-H.; Li, L.-J.; Wang, F. Ultrafast Generation of Pseudo-Magnetic Field for Valley Excitons in WSe_2 Monolayers. *Science* **2014**, *346*, 1205–1208.
10. Mak, K. F.; He, K.; Lee, C.; Lee, G. H.; Hone, J.; Heinz, T. F.; Shan, J. Tightly Bound Trions in Monolayer MoS_2. *Nat. Mater.* **2013**, *12*, 207–211.
11. Xu, X.; Yao, W.; Xiao, D.; Heinz, T. F. Spin and Pseudospins in Layered Transition Metal Dichalcogenides. *Nat. Phys.* **2014**, *10*, 343–350.
12. Lin, Y.; Ling, X.; Yu, L.; Huang, S.; Hsu, A. L.; Lee, Y.-H.; Kong, J.; Dresselhaus, M. S.; Palacios, T. Dielectric Screening of Excitons and Trions in Single-Layer MoS_2. *Nano Lett.* **2014**, *14*, 5569–5576.
13. Ruppert, C.; Aslan, O. B.; Heinz, T. F. Optical Properties and Band Gap of Single- and Few-Layer $MoTe_2$ Crystals. *Nano Lett.* **2014**, *14*, 6231–6236.
14. Yamamoto, M.; Wang, S. T.; Ni, M.; Lin, Y.-F.; Li, S.-L.; Aikawa, S.; Jian, W.-B.; Ueno, K.; Wakabayashi, K.; Tsukagoshi, K. Strong Enhancement of Raman Scattering from a Bulk-Inactive Vibrational Mode in Few-Layer $MoTe_2$. *ACS Nano* **2014**, *8*, 3895–3903.
15. Greenwood, N. N.; Earnshaw, A. *Chemistry of the Elements*; Pergamon Press: Oxford, 1984; p 911.
16. Pelant, I.; Valenta, J. *Luminescence Spectroscopy of Semiconductors*; Oxford University Press, 2012; pp 161−204.
17. Moulder, J. F.; Stickle, W. F.; Sobol, P. E.; Bomben, K. D. *Handbook of X-Ray Photoelectron Spectroscopy*; Perkin Elmer: MN, 1992; Vol. 40, p 63.
18. Jaros, M. A Case for Large Auger Recombination Cross Sections Associated with Deep Centers in Semiconductors. *Solid State Commun.* **1978**, *25*, 1071–1074.
19. Kresse, G.; Hafner, J. Ab Initio Molecular Dynamics for Liquid Metals. *Phys. Rev. B* **1993**, *47*, 558–561.
20. Kresse, G.; Furthmüller, J. Efficiency of Ab-Initio Total Energy Calculations for Metals and Semiconductors Using a Plane-Wave Basis Set. *Comput. Mater. Sci.* **1996**, *6*, 15–50.
21. Blöchl, P. E. Projector Augmented-Wave Method. *Phys. Rev. B* **1994**, *50*, 17953–17979.
22. Perdew, J. P.; Burke, K.; Ernzerhof, M. Generalized Gradient Approximation Made Simple. *Phys. Rev. Lett.* **1996**, *77*, 3865–3868.
23. Alfè, D. PHON, A Program to Calculate Phonons Using the Small Displacement Method. *Comput. Phys. Commun.* **2009**, *180*, 2622–2633.